Heat and Mass Transfer (2020) 56:797–810
https://doi.org/10.1007/s00231-019-02728-5

ORIGINAL

Numerical study of an impinging jet in cross-flow within and without influence of vortex generator structures on heat transfer

Ardalan Javadi[1]

Received: 25 January 2019 / Accepted: 10 August 2019 / Published online: 13 September 2019
© Springer-Verlag GmbH Germany, part of Springer Nature 2019

Abstract

An impinging jet heat transfer in cross-flow within and without influence of a vortex generator pair (VGP) is studied using the unsteady Reynolds averaged Navier-Stokes (URANS) and the large-eddy simulation (LES). The jet Reynolds number is 15,000 and the cross-flow Reynolds number is 30,000. The elliptic-blending Reynolds stress model (EBRSM) is implemented and adapted to capture the effect of the jet close to the wall. A $v^2 - f$ model is also implemented to study the ability in predicting such a benchmark. Both models benefit from the elliptic relaxation equation in the entire computational domain. The URANS results are compared with the accurate results of the LES method and also the experimental data. The URANS method successfully presents the flow features of the impinging jet while underpredicts the enhancing heat transfer over the channel bottom wall. The URANS method fails to correctly predict the flow structures forming around the impinging region, because the method is more diffusive than the LES method. When manipulating VGP, a rectangular winglet vortex generator pair is placed in the cross-flow channel and upstream of the jet nozzle to enhance the impinging heat transfer. The VGP increases the Nusselt number at the impingement region. The structures generated by the VGP alter the effects of the cross-flow on the impinging heat transfer. There are Kelvin-Helmholtz instabilities at the shear layer of the jet and the cross-flow in the base flow (the flow without VGP). These instabilities are altered in the flow with VGP. A swirl component is added in the jet to study the effects on the heat transfer. The result shows that for a high or moderate level of swirl, the jet is diffused before the impinging.

Keywords LES · URANS · Heat transfer · Vortex generator · Impingement cooling · Cross-flow

1 Introduction

Impinging jet provides an applicable means of high heat and mass transfer where management of locally augmented heat loading is required. It has been widely used in various industrial processes, which include heat transfer in gas turbines and electronic components, parts of the combustor in gas turbine engines, including combustion chamber liners, transition pieces, and splash plates, food industry, textile and paper, annealing of metals, and etc [1].

Impinging jets with special thermo-fluid characteristics are challenging for numerical simulations and they are indeed a recommended test-case for turbulence models to specially predict the flow features at the stagnation region. Most of investigations have been focused on axisymmetric round jets impinging normally on a flat surface [2]. A simple nozzle impinging jet implies three distinct regions through which fluid passes the free jet, the stagnation region and the radial wall-jet region, each featured by different prevailing turbulence dynamics and specific generic turbulence mechanisms [3]. The presence of a cross-flow which tends to deflect the impinging jet and degrade the favorable thermal performance of the impinging jet is even more challenging. The flow structure at low-velocity ratios (jet speed/cross-flow speed) might be fundamentally different from the common notion of shear-layer vortices, counter-rotating vortex pairs, wakes, and horseshoe vortices. Fluid in the near field is strongly accelerated, which affects the jet trajectory, entrainment, and mixing behavior [4]. To account for the effects of the cross-flow on the impingement cooling, the jet Reynolds

✉ Ardalan Javadi
ardalanjavadi@gmail.com; ardalan.javadi@uwaterloo.ca

[1] Mechanical and Mechatronics Engineering Department, University of Waterloo, 200 University Avenue West, Waterloo, ON N2L 3G1, Canada

number, the jet to cross-flow velocity ratio, and the nozzle-to-surface distance to jet diameter ratio are important parameters. Many investigations are carried out to increase the heat transfer of the jet impingement in cross-flow [5] while the heat transfer enhancements are accompanied with an additional pressure drop penalty [6]. Any effective method should be able to decrease the effects of the cross-flow on the jet like decreasing the Kelvin-Helmholtz instability (KHI).

Kelvin-Helmholtz instability (KHI) occurs at the interface of any two fluid streams in a state of relative motion or stratification. The flow dynamics underlying the three-stage development of KHI in low-speed shear layers highlighted by vortex roll-up and intense mixing between two streams is well established in literature [7]. Unsteadiness caused by the KHI is an important feature of single jet impingement, which creates challenges both for computational fluid dynamics prediction and experimental measurement. It is known that local flow streamline separations for a variety of different impingement configurations can result in KHI [8]. The growth of the KHI in the shear layer of impinging jets leads to the formation of roll-up vortices with a natural frequency mainly dependent on the nozzle-to-plate distance. The vortices generate pressure pulsations which affect the heat transfer in the stagnant region. The strength of these pulsations also depend on the nozzle to plate distance. In the presence of cross-flow, the shear from cross-flow around the jet affects the shear at of the jet edges. Thus, the KHI is completely different in the impinging jet in cross-flow from that which happens in the quiescent medium. Numerical approaches studying the impinging jets are widely treated in the literature with the purpose of assessing the ability of numerical simulations to capture the physical mechanism and of gaining insight on the physical phenomenon itself. The impinging jet is studied numerically, in particular using LES [2] to understand the flow features and to capture the thermal effects of impinging jets at different Reynolds numbers [9] while there is only a few detailed numerical investigations of impinging jet in cross-flow [10, 11]. Worth and Yang [12] reported some improvements of the Reynolds stress model (RSM) compared with the $k-\epsilon$ model for an impinging jet in a cross-flow. However the RSM fails to accurately predict the crescent shape vortex which wraps the impinging region and its location. They [12] finally concluded that RANS-based methods may only be suitable for preliminary design work.

The interaction of a cross-flow boundary layer with a jet is studied numerically [13, 14] and experimentally [15, 16] by different groups. Schlengel et al. [13] reported that a thicker approaching boundary layer leads to a deeper penetration of the jet. Thus, a rectangular winglet vortex generator pair (VGP) is placed in the jet exit upstream to promote the penetrate ration and enhance the impingement of the jet. Furthermore, a swirl component is added alongside the axial component in the jet to enhance the heat transfer. It is shown that a swirling jet increases the heat transfer from a flat surface [17] depending on the nozzle-to-surface distance to jet diameter ratio. Regarding the nozzle-to-surface distance to jet diameter ratio which is chosen to be 4, a moderate level of the swirl is expected to enhance the heat transfer. Wang et al. [1] recently studied the heat and the fluid flow of a jet impingement in cross-flow with and without different VGPs. They presented the jet flow features in cross-flow and concluded that a stronger impingement with higher wall-normal velocity and turbulent kinetic energy is produced with the VGP. The heat transfer is significantly augmented on the target wall [1].

A series of numerical simulation is carried out to replicate the engendered mechanism in impingement heat transfer in cross-flow. The turbulence models are studied and adjusted, a comprehensive mesh refinement study is presented for LES, the effect of a rectangular vortex generator pair is studied and the results of imposing a swirl component to the impinging jet is discussed. The paper is organized in different sections as the flow configuration is given in Section 2, the numerical details are presented in Section 3, which consists of two subsections for the base flow and the flow with the vortex generator pair. The results are discussed in the Section 4 including two subsections for the base flow and the flow with the vortex generator pair.

2 Flow configuration

As it can be seen in Fig. 1, a vortex generator pair (VGP) is placed on the top wall of the channel to enhance the jet impingement heat transfer. The VGP generates longitudinal vortices and these alter the upcoming cross-flow upstream of the jet. The VGP is with a thickness of 0.7 mm. Figure 2 shows a *xz*-view of the VGP orientation and the nozzle. Table 1 lists the used parameters in the present study. In the measurements, the jet exit axial velocity is fixed at $U_{axial,j} = 12$ m/s. This gives the jet Reynolds number $Re_j = 15,000$, based on the nozzle diameter of $d = 20$ mm. A tangential component is added on the jet velocity to produce swirl. The swirl quantity is comprehended using the *Sr* number [18] given by

$$Sr = \frac{1}{d}\frac{\int_0^d U_{\tan,j} U_{axial,j} r^2 dr}{\int_0^d U_{axial,j}^2 r dr}, \tag{1}$$

where $U_{\tan,j}$ and $U_{axial,j}$ are the tangential and axial velocity components of the jet, r is the radial position in the jet pipe. A tangential component of $U_{\tan,j} = 3$ m/s or 6 m/s, corresponding with the swirl number of 0.25 (referred, hereafter as S1) or 0.5 (referred, hereafter as S2),

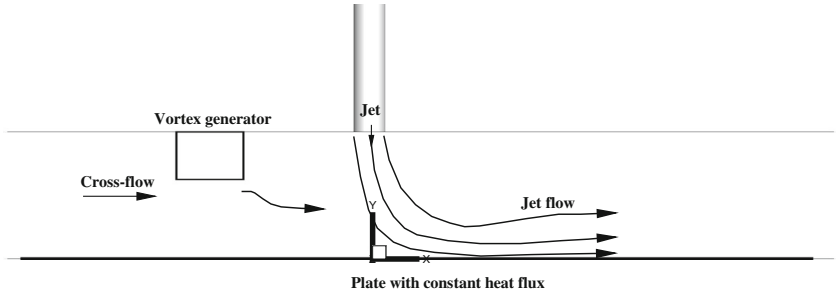

Fig. 1 The flow configuration and the computational domain in the on-axis xy-plane. The origin located on the heating plate and is aligned with the center of the jet. The thermal performance of an impinging jet in the cross-flow is studied and then a vortex generator pair (VGP) is placed in the upstream of the jet on the upper wall. The VGP effects on the heat transfer enhancing is discussed as well

respectively, is added on the jet velocity inlet to investigate the performance of the swirling jet on the heat transfer. The larger swirl number corresponds with the threshold of the on-axis recirculation region in a pipe flow [19, 20]. Capturing the physical mechanism engendered by the swirl is challenging for numerical modeling [21, 22] and a fine resolution is necessary to reasonably predict the radial pressure gradient generated by the swirl [19]. The cross-flow bulk velocity is fixed $U_c = 6$ m/s. This results in the cross-flow Reynolds number $Re_c = 30,000$ based on the channel height, $H_c = 80$ mm. Therefore, the ratio of the nozzle-to-surface distance to jet diameter to be $H_c/d = 4.0$. The experimental measurement reported by Wang [23] is done in a channel with 320 mm width. The jet to cross-flow velocity ratio is $U_{axial,j}/U_c = 2.0$. Both the jet and the cross-flow are kept at ambient temperature, T_0 [23].

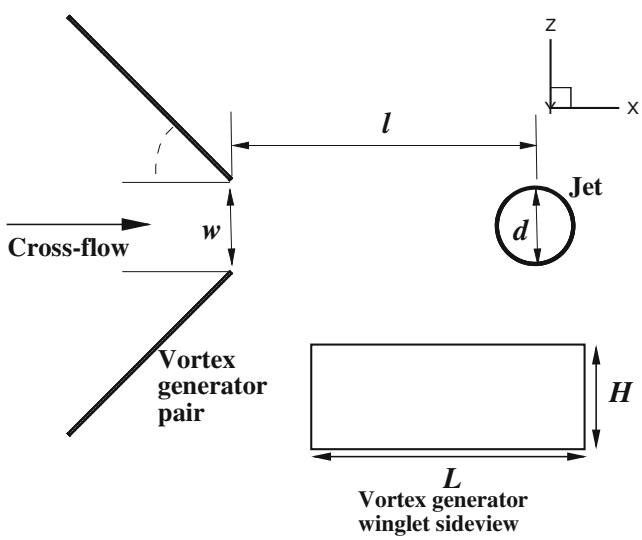

Fig. 2 The rectangular vortex generator pair orientation in a xz-plane. The dimensions of the rectangular VGP is shown in the bottom right of the figure

3 Modelling methodology

The simulations presented herein are performed using the finite-volume method in the OpenFOAM-3.0.x CFD code. The central differencing scheme is used for the diffusion terms. The second-order linear-upwind differencing is used for the URANS simulations to approximate the convection term. The unbounded central differencing scheme is also used for convective terms for the base flow when using LES. The limited linear total variation diminishing (TVD) scheme with a conformance coefficient is used for convective terms when using LES. The convection term is descretized using 5% second-order linear-upwind differencing and 95% central differencing. An implicit bounded second-order accurate Crank-Nicolson scheme is used to discretize the time terms. The computational domain is $L_y \times L_z = H_c \times 3H_c$ and is presented in Fig. 1. The domain is extended $L_x = 6H_c$ upstream of the jet and $L_x = 10H_c$ downstream of the jet to ensure that the boundary conditions are far from the impinging region. The origin is located on the heating plate on the bottom wall of the channel and is aligned with the center of the jet, see Fig. 1. Figure 3 shows the distribution of the two-point correlation along three spanwise lines. The most correlated spanwise line is at $(x, y) = (0, H_c/2)$ where the line crosses the jet and the VGP structures. As can be seen, the spanwise extent is sufficient to ensure the spanwise decorrelation.

Table 1 Setup parameters

Diameter of the jet nozzle	$d = 20$ mm
Length of the jet nozzle	$8d$
Rectangular winglet	$H = 1.5d, L = 2H$
Angle of attack	$\alpha = 45°$
Spacing between the VGP	$w = 1.2d$
Spacing between the VGP and the jet nozzle	$l = 4d$
Height of the channel	$H_c = 4d$

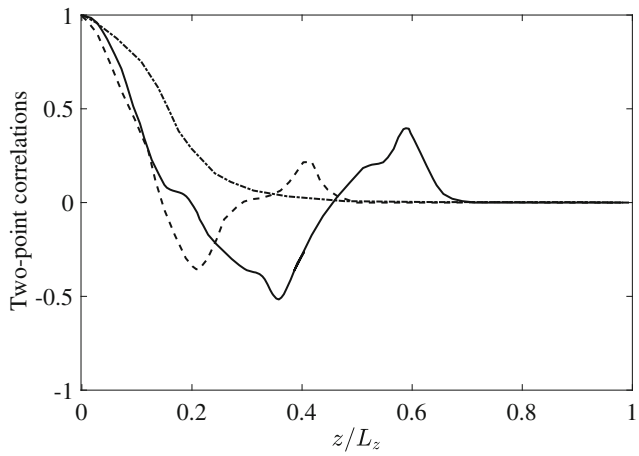

Fig. 3 Two-point correlations in the spanwise direction at $(x, y) = (0, H_c/2)$——, $(0, H_c/4)$ — —, $(-x/d = 4, H_c/2)$—.

The nozzle is extended $8d$ from the upper wall of the channel. The simulations are advanced in time with mean Courant-Friedrichs-Lewy (CFL) number of 0.06; therefore the local CFL number in the vicinity of the jet nozzle and close to the plate is smaller than one. The maximum CFL number is about 9, which happens locally close to the trailing edges of the VGP. The base flow which is impinging jet in cross-flow in the absence of VGP is studied with the URANS and LES methods. Two turbulence models, which benefit the elliptic blending model of Durbin [24], are used. He suggested that v^2 regarded as the turbulence stress normal to streamlines rather than k should be considered in computing the turbulent viscosity. Durbin's model enables the integration down to the wall, with an acceptable grid density without any damping function. A $v^2 - f$ model [25] is implemented and used which is proposed for incompressible and compressible flows, with a limit imposed on the turbulent viscosity. The elliptic-blending Reynolds stress model (EBRSM), proposed by Manceau and Hanjalić [26], is implemented [27] and verified in various flow fields. Thielen et al. [28] modified the EBRSM for a better performance in impinging jet flow field, which is used in this study. Moreover, the fluid is simulated with LES, the WALE (Wall Adapting Local Eddy viscosity) by Nicoud and Ducros [29] is chosen as sub-grid-scale model. The medium is air, treated as a compressible ideal gas. In LES the Navier-Stokes equation is expressed as

$$\rho\left(\frac{\partial \bar{u}_i}{\partial t} + \frac{\partial(\bar{u}_i\bar{u}_j)}{\partial x_j}\right) = -\frac{\partial \bar{p}}{\partial x_i} + \frac{\partial}{\partial x_j}\left(\mu\frac{\partial \bar{u}_i}{\partial x_j}\right) - \frac{\partial \tau_{ij}}{\partial x_j}, \quad (2)$$

where ρ is the air density, u is the velocity components, μ is the air absolute viscosity and p is the pressure. The turbulent stress tensor τ_{ij} is defined as

$$\tau_{ij} = \rho(\overline{u_i u_j} - \bar{u}_i\bar{u}_j). \quad (3)$$

The notation $<\bar{}>$ is used to show filtered values and $()_{ij}$ is index in physical space. The term in Eq. 3 is commonly modelled with a sub-grid-model based on the Bousinnesq approximation, relating the stress tensor to the local flow by the turbulent viscosity, μ_t, and the strain rate

$$\tau_{ij} - 1/3\tau_{kk}\delta_{ij} = 2\nu_t\bar{S_{ij}}. \quad (4)$$

In the study of impinging-jets' heat transfer in cross-flow, the thermal interaction due to the temperature gradient between the cross-flow and jet, and the wall are the main features of the flow. Thus, it is reasonable to choose the models and a sub-grid-model capable of accounting for near wall effects. The WALE model details are given here to be tuned. The definition of turbulent viscosity μ_t in the WALE sub-grid-scale model is

$$\mu_t = \rho\Delta^2\frac{(S^d_{ij}S^d_{ij})^{3/2}}{(\bar{S}_{ij}\bar{S}_{ij})^{5/2} + (S^d_{ij}S^d_{ij})^{5/4}}, \quad (5)$$

where Δ is the length scale (or grid filter) defined in terms of the cell volume V, locally changing as follows

$$\Delta = min(\kappa d_w, C_w V^{1/3}), \quad (6)$$

where κ is the von Kármán constant, d_w is cell distance from the wall and $C_w = 0.325$ and 0.525 is the switch coefficient. A higher level of modeled turbulence is expected with a higher C_w value. The switch coefficient is tuned to study its influence on the turbulent viscosity, μ_t. The strain tensors are defined as

$$\bar{S}_{ij} = \frac{1}{2}\left(\frac{\partial \bar{u}_i}{\partial x_j} + \frac{\partial \bar{u}_j}{\partial x_i}\right), \quad (7)$$

$$S^d_{ij} = \frac{1}{2}\left(\left(\frac{\partial \bar{u}_i}{\partial x_j}\right)^2 + \left(\frac{\partial \bar{u}_j}{\partial x_i}\right)^2\right) - \frac{1}{3}\delta_{ij}\left(\frac{\partial \bar{u}_k}{\partial x_k}\right)^2. \quad (8)$$

This sub-grid-scale model yields correct asymptotic behaviour near the wall and the sub-grid-scale eddy viscosity, ν_t, goes to zero without any *ad hoc* modifications or dynamic procedures. These qualities make the model well-suited for complex flows.

The energy equation is expressed as

$$\frac{\partial(\rho E)}{\partial t} + \frac{\partial(u_j\rho E)}{\partial x_j} = -\frac{\partial}{\partial x_j}\left(k\frac{\partial T}{\partial x_j}\right) - p\frac{\partial u_j}{\partial x_j} + \frac{\partial}{\partial x_j}(\tau_{ij}u_i), \quad (9)$$

where E is the total energy, T is the temperature and k is the thermal conductivity heat transfer coefficient. The turbulent Prandtl number was set to 0.9 and the viscous Prandtl number for air to 0.713.

3.1 The base flow

The domain is discretized with a fully structured and conformal body-fitted mesh using ICEM Hexa software.

The near wall region is resolved, the first cell spacing at the wall is 10^{-5} m ensuring y^+ smaller than one at any location and time for both methods. After a mesh independence study, the base flow (without VGP) is studied using 5.4 million cells for the URANS and 10.9 million cells for the LES. The resolution used for the URANS consists of $N_y \times N_z = 128 \times 128$ with $N_x = 144$ cells before the nozzle and $N_x = 160$ cells after the nozzle. The mesh used for the LES consists of $N_y \times N_z = 168 \times 232$ with $N_x = 224$ cells before the nozzle and $N_x = 96$ cells after the nozzle. The stretching ratio is 1.05 in the wall normal direction. The boundary conditions are discussed in the following section while the inflow conditions for two methods are reported herein. In order to match the inflow condition corresponding with the realistic conditions, the channel and the nozzle inflows are generated by a separate URANS and LES method. For the URANS method, the mean velocity, the turbulent kinetic energy and the Reynolds stresses tensor are captured and applied on the base flow. It is worth mentioning that the EBRSM is highly sensitive to its Reynolds stresses tensor profile at inlet. In LES, the velocity field in the channel and the pipe exit plane were recorded and stored at every time step. These data were subsequently used to define the inflow velocity components for the cross-flow simulation. It is worth mentioning that the domain before the nozzle could have been shorter due to the realistic inlet boundary condition. The domain is preserved the same for both methods.

The base flow is studied using two switch coefficients, $C_w = 0.325$ and 0.525 of the WALE model. Figure 4a shows the streamwise velocity fluctuation, $\overline{uu}/U_c^2$, of the base flow for different switch coefficients along the line $x/d = 1$. The streamwise velocity fluctuation is strong close to the top wall of the channel due to the interaction of the cross-flow and the jet nozzle. The peak around the channel center-line is due to the free shear layer between the leeward jet edge and the cross-flow. Figure 4b shows the viscosity ratio, ν_t/ν, of the base flow for different switch coefficients. The switch coefficient is shown by Eq. 6. If the resolution is fine the switch coefficient, C_w, will not play a prominent role. Figure 4 shows that a higher ν_t decreases the velocity fluctuation close to the wall. Since the resolution is fine enough to resolve the boundary layers, $C_w = 0.325$ is used to resolve more unsteadiness. Figure 5 shows the filter width along $x/d = 1$. It should be pointed out that the filter width at $x/d = 1$ is not smooth because of non-orthogonality of the resolution in the immediate downstream of the jet. The filter width changes smoothly close to the walls. Figure 4b shows that ν_t presents two peaks where the filter width increases.

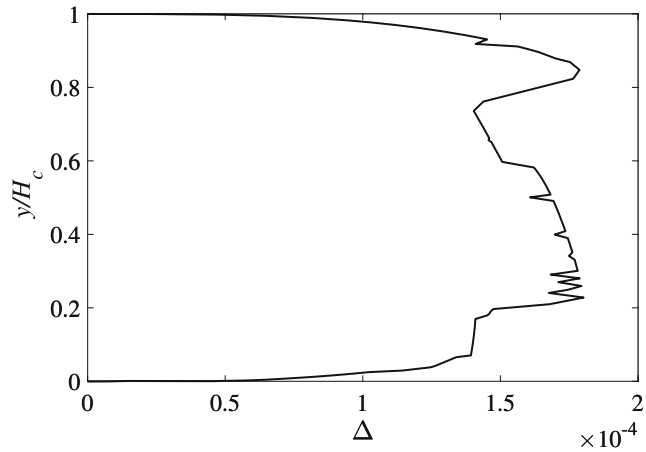

Fig. 5 The filter size, Δ (m), for the fine mesh, at $x/d = 1$ where the resolution is slightly non-orthogonal

3.2 The flow with VG

The domain is meshed using body-fitted grids in ICEM Hexa software. A detailed mesh refinement study is done because of lack of experimental results in the flow part. Three resolutions are used to carry out the mesh

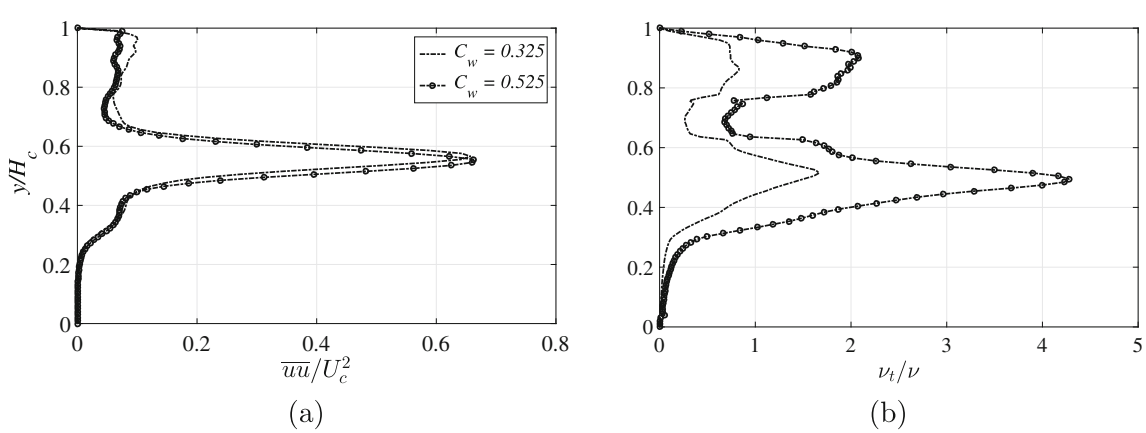

Fig. 4 **a** streamwise velocity fluctuation, $\overline{uu}/U_c^2$ at $x/d = 1$ in the on-center xy-plane, **b** Viscosity ratio, ν_t/ν, of the base flow for different switch coefficients, C_w, of the turbulence model of LES. The legend is the same for two subfigures

Table 2 Mesh resolution details in different sections of the domain including before VG, on VG, between VG and the jet and after the jet

	N_x before VG	N_x on VG	N_x in VG-jet	N_x after jet	total
coarse[a]	128	64	128	78	15×10^6
mid[b]	256	64	128	210	28×10^6
fine[c]	256	64	128	192	36×10^6

[a] $N_y \times N_z = 128 \times 256$, [b] $N_y \times N_z = 160 \times 272$, [c] $N_y \times N_z = 160 \times 304$

independence study, 15×10^6, 28×10^6 and 36×10^6 cells approximately. Table 2 shows the details of the resolutions. Regarding the stretching parameter chosen here, $1.2 \leq \Delta y^+ \leq 8$ and 14 grid points lay down within $y^+ \leq 10$, with the first point at $y^+ = 0.22$. The stretching ratio is 1.05 in the wall normal direction. The dimensionless distances in x and z directions are $\Delta x^+ = 18$ and $\Delta z^+ = 14$, respectively. Therefore, the requirements are fulfilled for a highly-resolved LES in a wall bounded flow.

Since the dominating factor of the mesh quality is the resolution in the near-wall region, some well established requirements of the grid spacing are necessary. The resolution can be assessed by comparing the size of a local grid spacing, G_s, and an estimate of the Kolmogorov length scale, η, which characterizes the length scale of the dissipative motion. The Kolmogorov scale is defined by the following expression

$$\eta = \left(\frac{\nu^3}{\epsilon}\right)^{\frac{1}{4}}, \tag{10}$$

where ν is the kinematic viscosity and ϵ is the dissipation rate. The dissipation is the summation of the resolved, ϵ_{res}, and modelled, ϵ_{sgs}, dissipation is defined by the following expression

$$\epsilon = \epsilon_{res} + \epsilon_{sgs}, \tag{11}$$

where the resolved part, ϵ_{res}, is calculated by

$$\epsilon_{res} = \nu \overline{\frac{\partial u_i}{\partial x_j}\frac{\partial u_i}{\partial x_j}}, \tag{12}$$

and the modeled part, ϵ_{sgs}, is calculated by

$$\epsilon_{sgs} = \frac{C_E k_{sgs}^{\frac{3}{2}}}{G_s}, \tag{13}$$

where k_{sgs} is the sub-grid-scale kinetic energy and C_E is an empirical constant, $C_E = 0.7$. The empirical constant is considered as 1.0 by Schumann [30] while it overpredicts the actual dissipation rate. Furthermore an estimate of k_{sgs} is typically calculated from

$$k_{sgs} = \left(\frac{\nu_{sgs}}{C_\nu G_s}\right)^2, \tag{14}$$

where ν_{sgs} is the computed sub-grid-scale viscosity and C_ν is another empirical constant. It should be noted that some dispute on the reasonable magnitude of the C_ν constant do exist in the literature. Since the resolution in this study is fine, $C_\nu = 0.094$ is considered. Results showing the spatially and temporally averaged G_s/η before and after the nozzle for the fine mesh are presented in Fig. 6.

It is argued by Pope [31] that in an isotropic turbulence the maximum dissipation takes place at length scales of about 24η. As at least two points are necessary to resolve any flow feature, a grid spacing of 12η is needed to resolve the scale of 24η. Thereby, any flow region discretized by cells with $G_s/\eta \leqslant 12$ can be considered as very well resolved. Inspecting the results presented in Fig. 6, it can be seen that maximum G_s/η ratio does not exceed 12, indicating that the presently used grid resolution is very fine resolved LES (Fig. 7).

The Neumann boundary condition is applied at the outlet boundary for the velocity and the negative velocities are clipped. The no-slip wall boundary condition is applied on the bottom and the top walls, the VGP and the nozzle wall. The slip boundary condition is applied on the spanwise direction. The inlet boundary condition for the channel is a fully developed channel flow mean velocity profile. The channel inlet boundary condition is challenging because the flow feels the presence of the VGP far upstream. The recycling method [32] was not successful to replicate the flow field. This method, which was developed for flat-plate

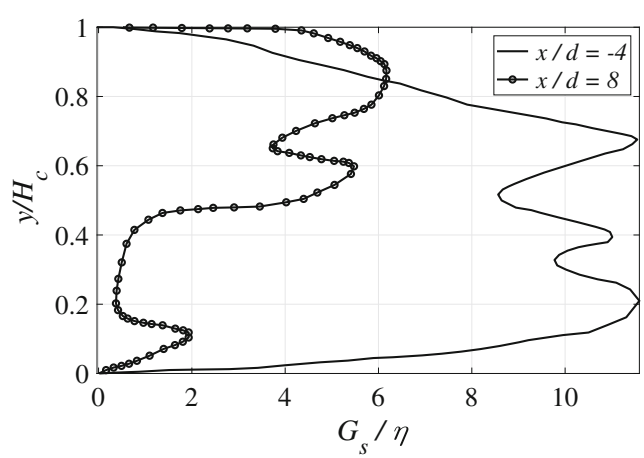

Fig. 6 Estimate of the spatially and temporally averaged G_s/η ratio in yz-plane for the fine mesh, $x/d = -4$ is placed between to trailing edge of the VGP

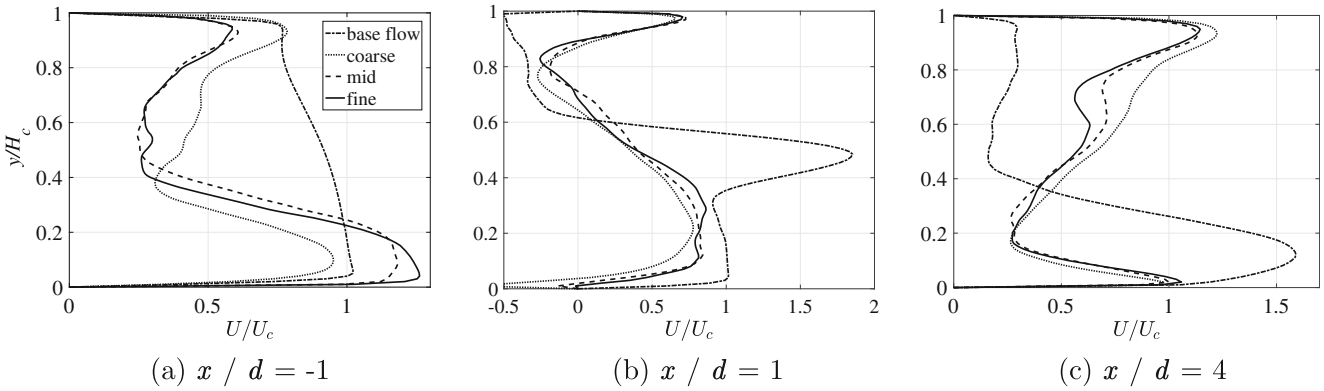

Fig. 7 The streamwise velocity for the flow with VGP using three meshes in the on-center xy-plane. The base flow is also presented for comparison. The legend is the same for all subfigures

boundary layers, consists of taking a plane of data from a location several boundary-layer thickness downstream of the inflow, and rescaling the inner and outer layers of velocity profiles separately, to account for the different similarity laws that are observed in these two regions. In order to match the inflow condition corresponding with the realistic conditions, the channel inflow is generated by a separate LES simulation of the fully developed turbulent channel flow. The velocity field in the channel exit plane was recorded and stored at every time step. These data were subsequently used to define the inflow velocity components for the cross-flow simulation. Imposing mean velocity with superimposed pseudo turbulent fluctuations, generated by a method presented by Klein, Sadiki and Janicka [33] was also successful to replicate the impinging region. The length scales at the inflow of the channel is set to $0.125H_c/2$ and the fluctuation level to a uniform value of 2%. The inlet boundary condition for the jet generated using the recycling method for velocity. The inlet boundary condition for the swirling jet is constant axial and tangential mean velocity with superimposed pseudo turbulent fluctuations, generated by a method presented by by Klein, Sadiki and Janicka [33]. The idea is to filter random data in order to obtain prescribed two point correlations together with a prescribed Reynolds stress tensor. The turbulence intensity for the swirling jet corresponds with that of the non-swirling jet at the jet exit. The length scales at the inflow of the jet nozzle is set to $0.125d/2$ and the fluctuation level to a uniform value of 2%.

4 Results and discussions

4.1 The base flow

The base flow is discussed in this section by validating the numerical results of the URANS method with the highly-resolved LES. Figure 8 validates the streamwise Nusselt number over the plate in the on-center xy-plane. The heat transfer coefficient is calculated as

$$h = \frac{Q_w}{T_w - T_0}, \tag{15}$$

where Q_w is the total heat flux imposed on the plate, T_w is the wall temperature and T_0 is the air bulk temperature. Based on the jet diameter, d, the Nusselt number is defined

$$Nu = \frac{hd}{k}, \tag{16}$$

where h is the air convective heat transfer and k is the air thermal conductivity coefficient. The LES shows a good agreement with the measurements. The impinging location based on the maximum Nusselt number, $Nu_{\max} = 48$, is at $x/d = 5.8$. The LES slightly overpredicts the Nu at $x/d = 5.8$, $Nu = 50$, while the maximum Nu predicted by LES is 51 ($x/d = 5.5$). The URANS method underpredicts the Nusselt number. The impingement offered by the EBRSM is

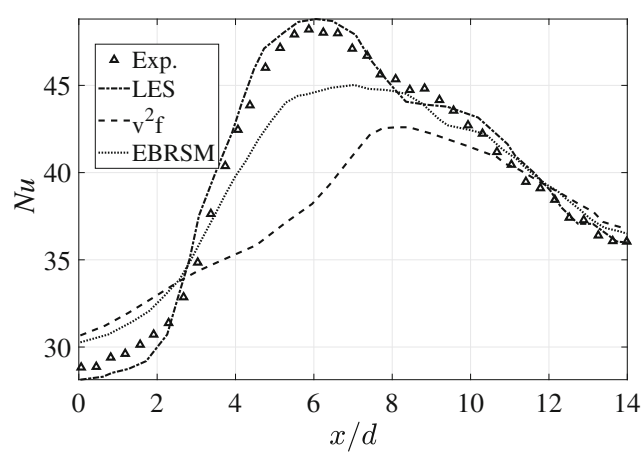

Fig. 8 The streamwise Nusselt number variation for the base flow on the heating plate in the on-center xy-plane. The experimental results are taken from ref. [23]

around $x/d = 6$ with $Nu = 45$. The $v^2 - f$ model captures the impingement around $x/d = 8$ with $Nu = 42$. The EBRSM is less diffusive than the $v^2 - f$ model; therefore, it predicts +6.25% maximum *Nu* number than that of the $v^2 - f$ model. Since the EBRSM exactly solves the production terms, it can selectively augment or damp the stresses due to the curvature effects, the swirl and the stagnation. It means that the EBRSM captures more realistic structures around the impinging region. Figure 9 shows the streamwise and wall-normal mean velocity of different methods before and after the nozzle. Figure 9a shows that the velocity profile of the URANS method in the jet upstream is still very much fully developed while the LES sees the jet more remarkable. Therefore, the cross-flow predicted by the URANS deflects the jet more than that of the LES. Figure 9b shows that the wall-normal velocity before the nozzle is almost negligible. In the near downstream of the jet, Fig. 9c, the EBRSM yields better results than that of the $v^2 - f$ model close to the top and the bottom channel wall. Figure 9e shows the strong downward flow of the jet. Figure 10 shows the streamwise velocity fluctuation after the jet. The EBRSM results are very close to the LES ones while the $v^2 - f$ model underpredicts the velocity fluctuations after the jet. The $v^2 - f$ model is initialized by the Launder-Sharma $k - \epsilon$ model and the EBRSM is initialized by the Speziale-Sarkar-Gatski (SSG) Reynolds stress model. The elliptic relaxation equation used by the URANS turbulence models improves the results significantly.

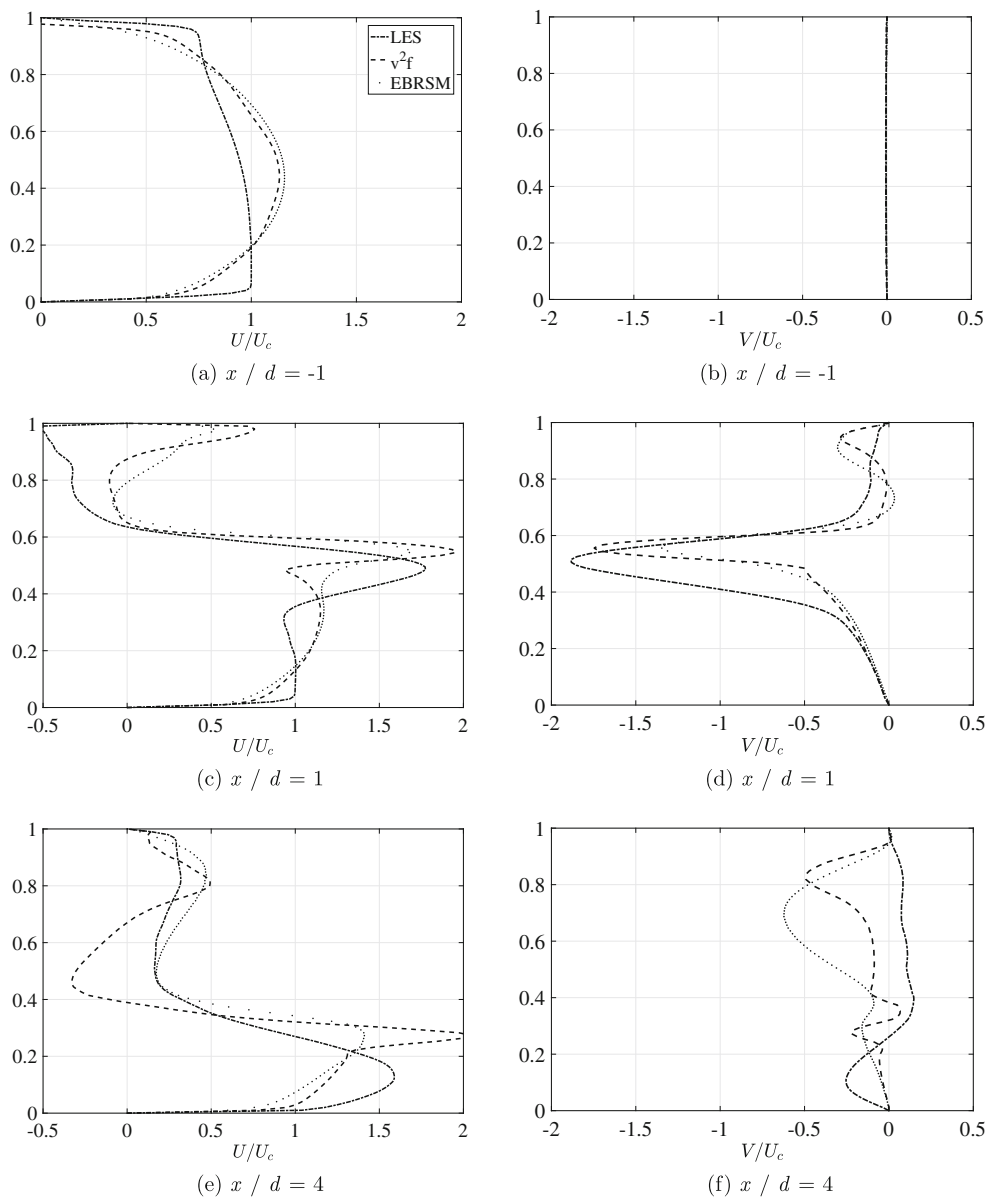

Fig. 9 The velocity components for the base flow with different turbulence models in the on-center xy-plane

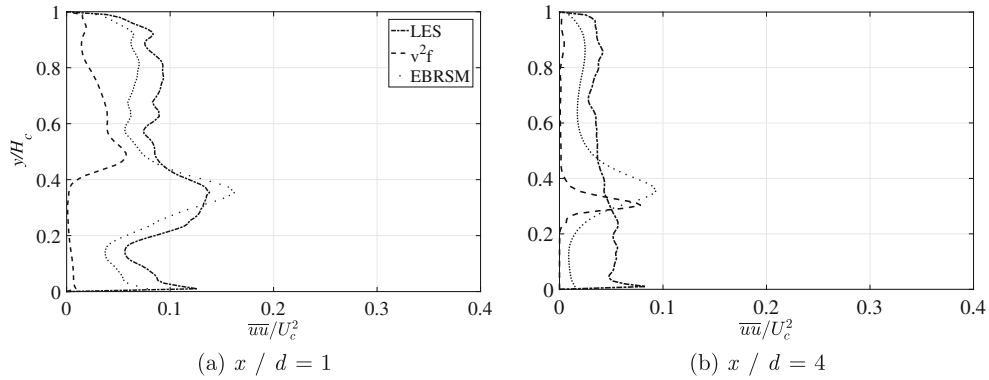

Fig. 10 The streamwise velocity fluctuation for the base flow with different turbulence models in the on-center xy-plane. The legend is the same for all subfigures

4.2 The flow with VG

The computational domain is appropriately extended upstream of the VGP. Figure 7 shows minor discrepancies among the mean velocities that are captured using different resolutions. The velocity profiles of the mid and the fine resolution are very close. The VGP strongly perturbs the upper wall boundary layer far upstream. Placing a vortex generator upstream of a jet is imperative for the enhancement of the heat transfer. Figure 11 shows the heat transfer coefficient in the streamwise direction on the plate in the on-center xy-plane. It shows the LES results together with the experimental measurements. The maximum values are predicted very well in the base flow and the flow with the VGP. The maximum $Nu = 48$ ($x/d = 5.8$) is measured for the base flow while the LES yields $Nu = 50$ at that location. The maximum $Nu = 110$ ($x/d = 0.9$) is measured for the flow with the VGP while the LES yields $Nu = 106$ at that location. The maximum Nu given by LES is 115 ($x/d = 1.6$). The difference between the numerical Nusselt numbers and the experimental ones might be related to the non-orthogonality of the resolutions around the VGP. Imposing a swirl component in the jet in this flow configuration does not enhance the impinging heat transfer. However, the peak of Nu number for S1 is larger than that of S2. As it is mentioned before, the jet in S2 losses its coherence quicker than that of S1. The LES results underpredict the Nu number downstream of the impingement.

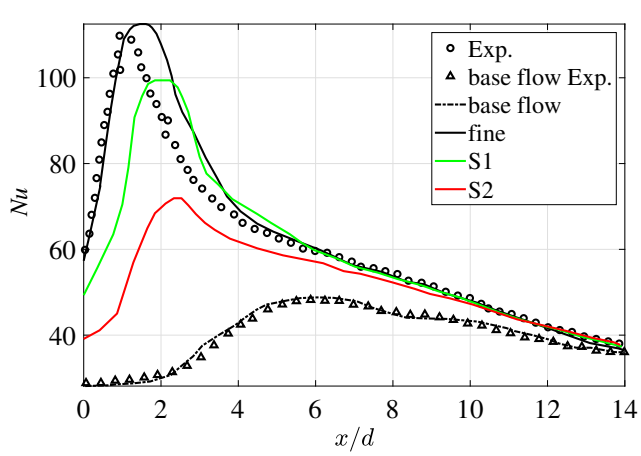

Fig. 11 The streamwise Nusselt number variation on the heating plate in the on-center xy-plane. The experimental results are taken from ref. [23]

The mean Nusselt number, $\overline{Nu}$, calculated by

$$\overline{Nu} = \frac{\int_{-3d}^{3d}\int_{0}^{10d} Nu(x,z)dxdz}{A}, \tag{17}$$

where A is the total area between $0 < x/d < 10$ and $-3 < z/d < 3$ on the impingement wall [34].

The pressure drop of the jet (ΔP_j) is measured from two points located at x/d = - 24.0 and 30.5. The pressure drop of the cross-flow (ΔP_c) is measured from two points located at $x/d = -12.5$ and 30.5. Based on the average heat transfer and pressure drop of the jet, the thermal performance is also calculated by $\overline{Nu}/\Delta P_j^{1/3}$. The experimental results presents $\overline{Nu}/\Delta P_j^{1/3} = 7.88$ for the base flow and $\overline{Nu}/\Delta P_j^{1/3} = 11.84$ for the flow with the VGP while the numerically predicted values are 7.97 and 12.03, respectively. Placing the VGP enhances the heat transfer by +63.6% while increases the pressure drop by +29.0%. The thermal performance of the jet increases by +50.2% with placing the VGA. The LES predicts this enhancement very well. Table 3 summarizes the numerical results and the experimental measurements.

The Fig. 12(top) shows the high vortical regions of the flow. It can be seen that the impinging occurs about $x/d = 1$ on the plate. A horse-shoe vortex forms around the impingement region, where is encirculated to highlight the structures. The cross-flow wraps the jet to form a horse-shoe vortex close to the plate. As a result, two streamwise counter-rotating vortices develop side-to-side and decay further downstream of impinging region. The nature of each ground vortex is similar to the crescent shape structure known to be generated by the deflection of a boundary layer by a solid obstacle [35]. There is a pocket of high vorticity region on the suction side of

Table 3 Average heat transfer and pressure drop of the jet impingement in cross-flow within and without VGP. The experimental results are taken from ref. [23]

-	$\overline{Nu}$	ΔP_j (Pa)	ΔP_c (Pa)	$\overline{Nu}/\Delta P_j^{1/3}$
base flow	32.7	71.56	6.78	7.88
LES of base flow	33.0	71.04	6.71	7.97
flow with VGP	53.5	92.32	10.48	11.84
LES of flow with VGP	55.1	96.08	11.61	12.03

the VG winglet. Figure 12(bottom) shows the streamlines in different planes. The vortical structures generated by VGP are pushed downward by the jet and retain their coherence far downstream. α shows the horse-shoe vortex in the upstream of the impingement and β shows the crescent shape structure around the nozzle. Figure 13 shows the iso-surface of Q-criterion. The horse-shoe vortex and the crescent shape structure, which is the result of the interaction between the cross-flow and the jet, are presented.

Figure 14 shows the y-vorticity, $\vec{\omega}_y = (\nabla \times \vec{U})_y(\frac{1}{s})$, along cross-section plane $y = H_c/4$ for the flows with and without VGP. Dipole structures associated with the formation and development of the Kelvin-Helmholtz vortices is also apparent in Fig. 14(top). It can be seen that there are two counter-rotating vortices generated in the downstream of the jet in the base flow. The vortices retain their coherence far downstream. These is no large coherent structures at the cross-section plane y = $H_c/4$ in the flow with the VGP, see Fig. 14(bottom).

Figure 15 shows the streamwise and wall-normal mean velocity of different flows. The streamwise velocity, U/U_C, in the channel is strong close to the bottom wall before the jet and is strong close to the top wall after the jet for the flow with the VGP. The flow wraps the jet and goes up to the top wall of the channel; therefore the VGP reduces the effects of the cross-flow on the impinging jet. Figure 15b shows the strong downward flow due to the VGP. Figure 15c clearly shows that the jet impinges about $x/d = 1$ on the plate for the flows with the VGP while the jet in the base flow impinges more downstream, about $x/d = 6$. The base flow feels the jet, and leaves the pattern of the fully developed flow far upstream, see Fig. 15a. A negative velocity region can be seen at $x/d = 1$ around $y/H_c \sim 0.8$ due to the wake of the jet in the cross-flow, see Fig. 15c. The streamwise velocity of the flow with the VGP is very similar with those of S1 and S2 before the nozzle. The streamwise velocity of S2 at $x/d = 1$ is different close to the bottom wall of the channel due to the relatively high level of swirl in the jet. There is strong downward flow before and after the nozzle due to the VGP.

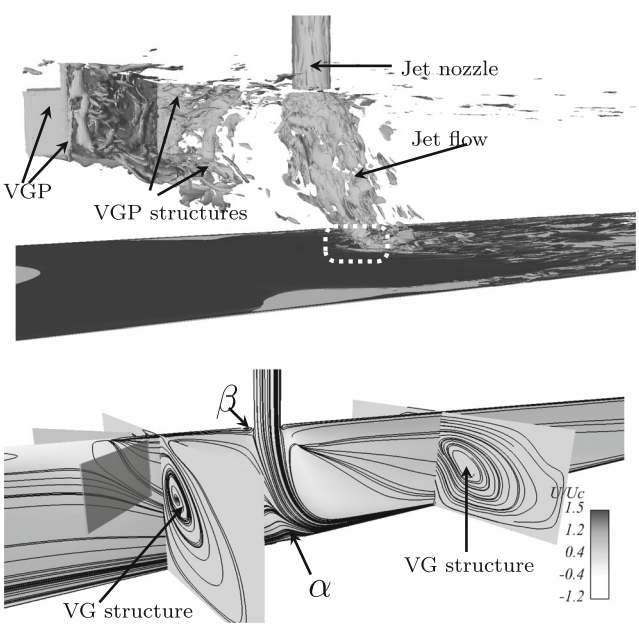

Fig. 12 top) Iso-surface of vorticity in the vicinity of the VGP and the jet nozzle, the encirculated region shows the impingement region where is about $x/d = 1, d = 20$ mm. bottom) streamlines in the on-center xy-plane and two yz-planes. The on-center plane is colored by the streamwise mean velocity. α points the horseshoe vortex around the impingement region. β points the crescent shape structures around the jet nozzle

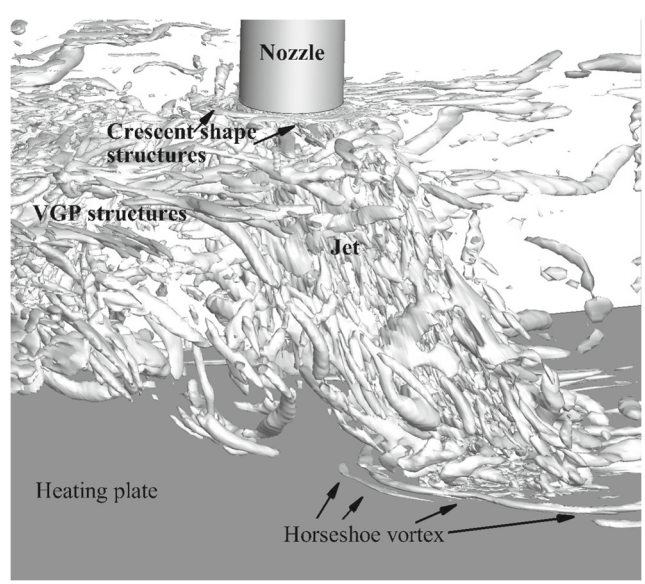

Fig. 13 The iso-surface of Q-criterion

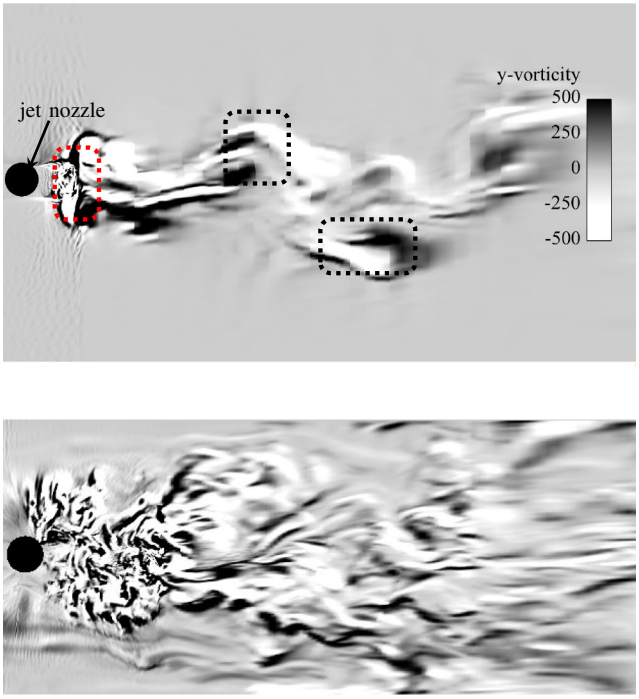

Fig. 14 Instantaneous y-component vorticity, $\vec{\omega}_y = (\nabla \times \vec{U})_y(\frac{1}{s})$, along cross-section plane $y = H_c/4$. top) Kelvin-Helmholtz vortices are generated by the interaction of the cross-flow and the jet in the base flow. The jet core is encirculated by red box and Kelvin-Helmholtz vortices are at two downstream corners of the red box. The dipole vortices are encirculated by black boxes. bottom) KHI is not detected in the flow with VG

The highest level of turbulence happens close to the trailing edge of the winglet. Figure 16 shows the velocity fluctuations mean square in the on-center xy-plane after the jet, at $x/d = 1$ and 4. The base flow gives a peak about the center-line of the channel due to the shear layer at the leeward edge of the jet, see Fig. 16a. The peaks of $\overline{uu}/U_c^2$ close to the bottom wall is due to the wall-jet. It can be seen that the flow with the VGP yields the strongest peak and then those of S1 and S2. Figure 16b shows that $\overline{uu}/U_c^2$ of the flows with the VGP is stronger than that of the base flow even at $x/d = 4$. This is another reason that the heat transfer is enhanced due to the VGP structures. The strong swirling jet, S2, yields a weaker peak of $\overline{uu}/U_c^2$ which the peak is slightly shifted upward. The S2 jet losses its coherence earlier than that of S1. Figure 16c presents $\overline{uv}/U_c^2$ with three negative peaks which the top one is due to the interaction of the cross-flow and the nozzle flow; the mid one, which is also the largest one, is due to the VGP structures and the wake behind the jet; the bottom one is due to the wall-jet. The base flow presents two peaks of $\overline{uv}/U_c^2$ which the larger one is due to the shear layer of the leeward edge of the jet. Figure 16d shows two negative peaks for the flows with the VGP while the wall-jet peak turned positive. Based on the shear layer peaks, the vortical structures generated by the VGP make an angle of 6° with the channel center-line. It is worth mentioning that the streamwise and wall-normal velocity fluctuations are negatively correlated in the wake of the jet; therefore, a negative v carries high momentum fluid away from the channel center-line. This negative correlation should be promoted to decrease the effect of the cross-flow on the impingement cooling and enhance the heat transfer. This is the reason that the streamwise velocity in the downstream gives a large peak close to the top wall, see Fig. 7b and c. Figure 16e presents a peak of $\overline{ww}/U_c^2$ close to the top wall of the channel which is diffused in the downstream. The flow goes toward the steady condition further downstream.

A complete description of a turbulent variable u at a given location and instant in time is given by the probability density function (PDF), $f(u)$, where $f(u)$ is

$$\int_{-\infty}^{+\infty} f(u)du = 1. \tag{18}$$

The *skewness* is the third moment of u, normalized by u_{rms}^3,

$$S = \frac{1}{u_{rms}^3}\int_{-\infty}^{+\infty} u^3 f(u)du = \frac{1}{2u_{rms}^3}\int_{-T}^{T} u^3(t)dt. \tag{19}$$

The variance (the square of RMS) shows how large the fluctuations are in average, but it does not present if the time history includes few very large fluctuations or if all are rather close to velocity fluctuation root mean square. The *flatness* gives this information, and it is defined from u^4 and normalized by u_{rms}^4, i.e.

$$F = \frac{1}{u_{rms}^4}\int_{-\infty}^{+\infty} u^4 f(u)du. \tag{20}$$

Figure 17 shows the probability density function (PDF) at two point in the on-center xy-plane. The first is located close to the top wall and between the VGP at $x/d = -4$. The skewness is $S = 4$ and the flatness is $F = 0.4$. Figure 17a shows that the values are approximately equally distributed around zero. There exists some large positive values and some large negative values. The absolute value of the positive ones are larger that of the negative ones while the number of negative values is higher than their counterparts. The second point is located at the impingement at $x/d = 1$. The skewness is $S = -2$ and flatness is $F = 9$. Figure 17b shows that the most of values are positive while there are some large negative values. The PDF confirms that there are a few large positive values, which shows 3-dimensionality of the flow at the impingement. The PDF of other components are very similar to Fig. 17.

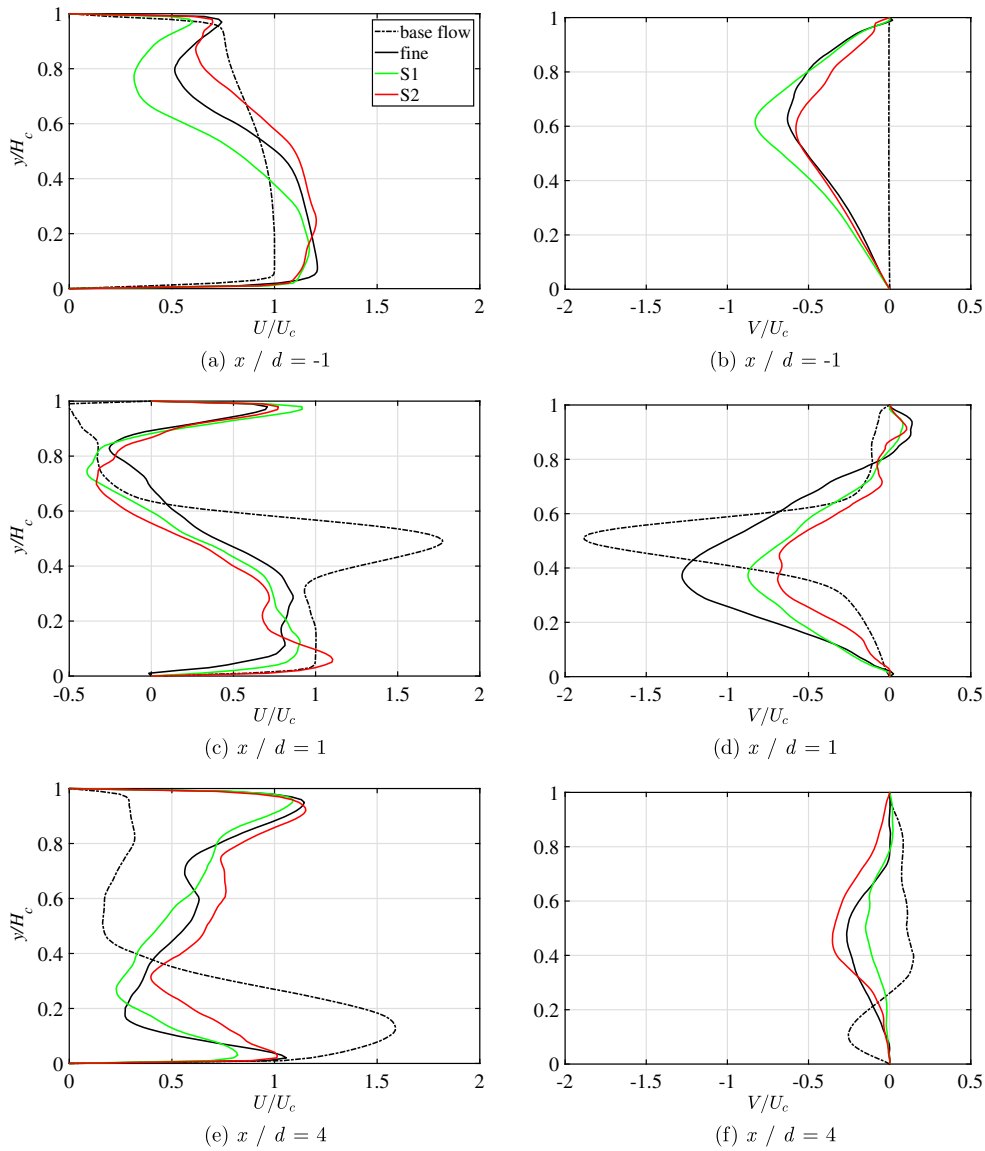

Fig. 15 The velocity components for different flows, the base flow, with VGP and with swirling jet in the on-center xy-plane. The legend is the same for all subfigures

5 Conclusion

Numerical study of impinging heat transfer in cross-flow within and without influence of a vortex generator pair (VGP) is undertaken. The URANS and LES methods are used to study the base flow while the flow with VGP is studied with the LES. The URANS turbulence models benefit from the elliptic relaxation equation. They successfully predict the main features of the impinging jet in the cross-flow, while they predict a slightly more deflected jet. Furthermore, they undervalue the *Nu* number. The EBRSM presents the *Nu* number with -6.25% error. The $v^2 - f$ model underpredicts the *Nu* number with -12.5% error. The LES results predict the convective heat transfer in the base flow and the heat transfer enhancing in the flow with the VGP with reasonable agreement with the measurements. The VGP generates strong structures which make the flow to get around the jet and move upward to the top wall of the channel. Thus, the VGP decreases the drawback of the cross-flow on the impinging heat transfer. Placing the VGP enhances the heat transfer by $+63.6\%$ while gives $+29.0\%$ higher pressure drop. The thermal performance of the jet increases by $+50.2\%$ with manipulating the VGA. The LES predicts this enhancement very well. The Kelvin-Helmholtz instabilities are strong in the base flow while the VGP avoid generating the instabilities in the shear layers. However, the jet hits the heating plate with a higher level of turbulence in the presence of the VGP than that of the base flow, which this increases the 3-dimensionality of the impinging jet. A swirl component is added in the jet to study the effects of the swirling jets on the heat transfer. The swirling jets lose their coherence before the impingement, therefore, they do not enhance the *Nu* number.

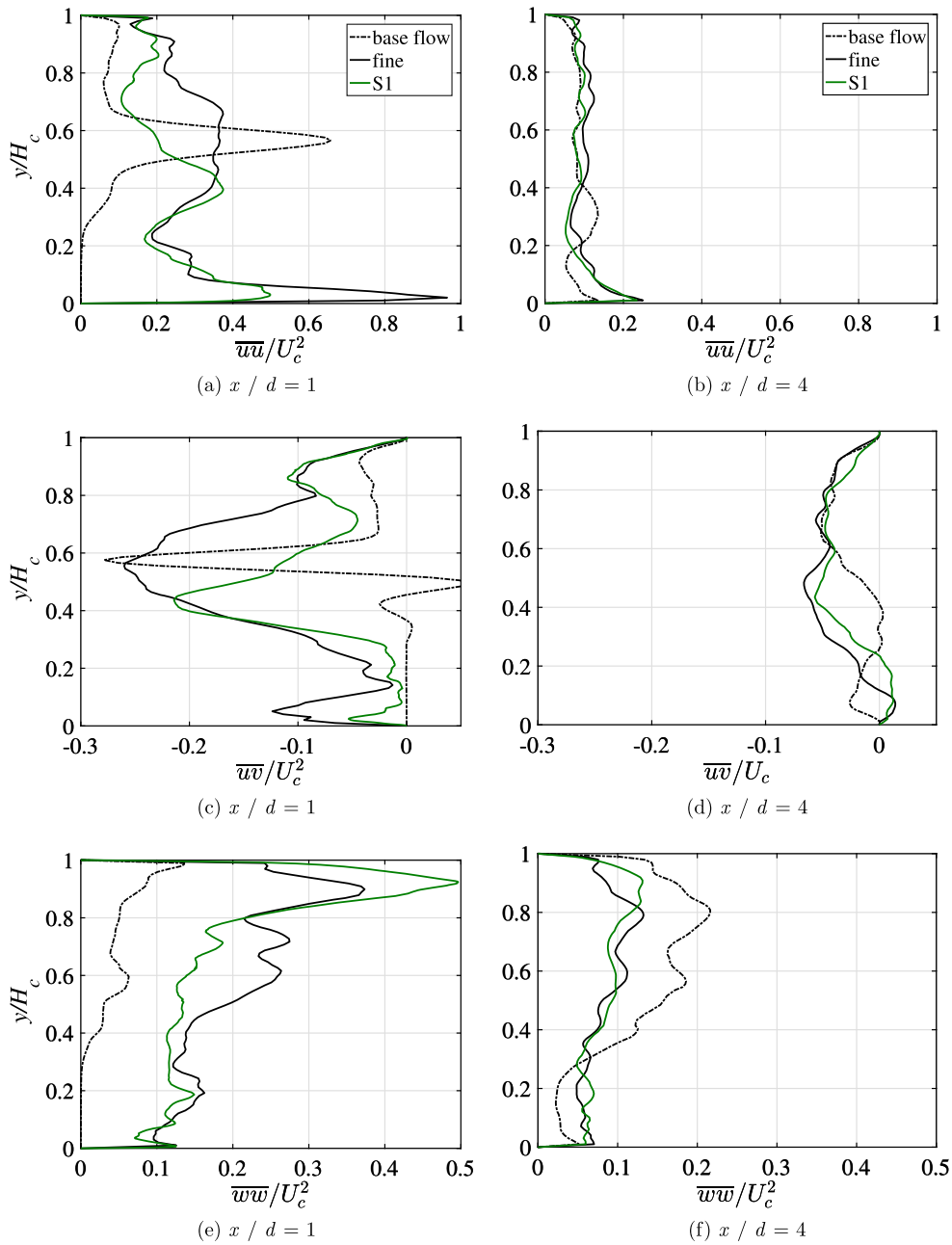

(a) x / d = 1 (b) x / d = 4

(c) x / d = 1 (d) x / d = 4

(e) x / d = 1 (f) x / d = 4

Fig. 16 The velocity fluctuation for different flows, the base flow, with VGP and with swirling jet in the on-center xy-plane. The legend is the same for all subfigures

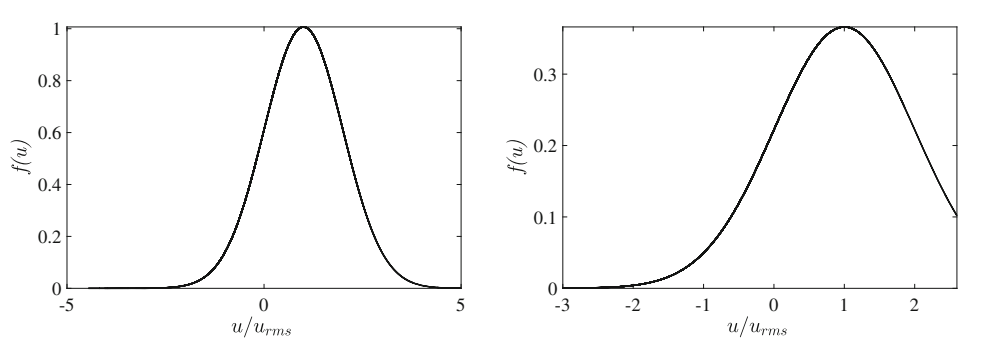

(a) at x / d = -4 adjacent to the top wall (b) at x / d = 1 adjacent to the bottom wall

Fig. 17 The probability density function (PDF) for the fine resolution before and after the nozzle in the on-center xy-plane

References

1. Wang C, Wang Z, Wang L, Luo L, Sundén B (2019) Experimental study of fluid flow and heat transfer of jet impingement in cross-flow with a vortex generator pair. Int J Heat Mass Transfer 135:935–949
2. Hadžiabdić M, Hanjalić K (2008) Vortical structures and heat transfer in a round impinging jet. J Fluid Mech 596:221–260. https://doi.org/10.1017/S002211200700955X
3. Chauhan R, Singh T, Thakur N, Kumar N, Kumar R, Kumar A (2018) Heat transfer augmentation in solar thermal collectors using impinging air jets: a comprehensive review. Renew Sust Energ Rev 82:3179–3190
4. Mahesh K (2013) The interaction of jets with crossflow. Annu Rev Fluid Mech 45:379–407
5. Liu Y-H, Song S-J, Lo Y-H (2013) Jet impingement heat transfer on target surfaces with longitudinal and transverse grooves. Int J Heat Mass Transf 58(1):292–299. https://doi.org/10.1016/j.ijheatmasstransfer.2012.11.042
6. Zuckerman N, Lior N (2006) Jet impingement heat transfer: physics, correlations, and numerical modeling. Adv Heat Tran 39:565–631. https://doi.org/10.1016/S0065-2717(06)39006-5
7. Caulfield C, Peltier W (2000) The anatomy of the mixing transition in homogeneous and stratified free shear layers. J Fluid Mech 413:1–47
8. Lugt HJ (1983) Vortex flow in nature and technology, vol 1. Wiley-Interscience, New York, p 305. Translation., 1983. https://doi.org/10.1017/S0022112084221447
9. Uddin N, Neumann SO, Weigand B (2013) LES simulations of an impinging jet: on the origin of the second peak in the nusselt number distribution. Int J Heat Mass Transf 57(1):356–368. https://doi.org/10.1016/j.ijheatmasstransfer.2012.10.052
10. Yang L, Ren J, Jiang H, Ligrani P (2014) Experiment al and numerical investigation of unsteady impingement cooling within a blade leading edge passage. Int J Heat Mass Transf 71:57–68. https://doi.org/10.1016/j.ijheatmasstransfer.2013.12.006
11. Xing Y, Spring S, Weigand B (2011) Experimental and numerical investigation of impingement heat transfer on a flat and micro-rib roughened plate with different crossflow schemes. Int J Therm Sci 50(7):1293–1307. https://doi.org/10.1016/j.ijthermalsci.2010.11.008
12. Worth NA, Yang Z (2006) Simulation of an impinging jet in a crossflow using a Reynolds stress transport model. Int J Numer Methods Fluids 52(2):199–211
13. Schlegel F, Wee D, Marzouk YM, Ghoniem AF (2011) Contributions of the wall boundary layer to the formation of the counter-rotating vortex pair in transverse jets. J Fluid Mech 676:461–490. https://doi.org/10.1017/jfm.2011.59
14. Javadi A, El-Askary WA (2012) Numerical prediction of turbulent flow structure generated by a synthetic cross-jet into a turbulent boundary layer. Int J Numer Methods Fluids 69(7):1219–1236. https://doi.org/10.1002/fld.2632
15. Zang B, New TH (2017) Near-field dynamics of parallel twin jets in cross-flow. Phys Fluids 29(3):035103
16. Karagozian AR (2014) The jet in crossflow. Phys Fluids 26(10): 1–47
17. Wen M-Y, Jang K-J (2003) An impingement cooling on a flat surface by using circular jet with longitudinal swirling strips. Int J Heat Mass Transf 46(24):4657–4667. https://doi.org/10.1016/S0017-9310(03)00302-8
18. Gupta AK, Lilley DG, Syred N (1984) Swirl flows. Abacus Press, Tunbridge Wells, p 488
19. Javadi A, Nilsson H (2015) LES and DES of strongly swirling turbulent flow through a suddenly expanding circular pipe. Comput Fluids 107:301–313. https://doi.org/10.1016/j.compfluid.2014.11.014
20. Javadi A, Bosioc A, Nilsson H, Muntean S, Susan-Resiga R (2016) Experimental and numerical investigation of the precessing helical vortex in a conical diffuser, with rotor–stator interaction. ASME J Fluids Eng 138(8):081106. https://doi.org/10.1115/1.4033416
21. Javadi A, Nilsson H (2015) Time-accurate numerical simulations of swirling flow with rotor-stator interaction. Flow Turbul Combust 95(4):755–774. https://doi.org/10.1007/s10494-015-9632-2
22. Javadi A, Nilsson H (2017) Detailed numerical investigation of a Kaplan turbine with rotor-stator interaction using turbulence-resolving simulations. Int J Heat Fluid Flow 63:1–13. https://doi.org/10.1016/j.ijheatfluidflow.2016.11.010
23. Wang C (2016) Experimental study of outlet guide vane heat transfer and gas turbine internal cooling, Ph.D. thesis, Lund University. https://lup.lub.lu.se/search/publication/dbf4ad95-1adb-4f3a-bfb4-4958f166213e
24. Durbin PA (1991) Near-wall turbulence closure modeling without damping functions. Theor Comput Fluid Dyn 3(1):1–13
25. Lien F-S, Kalitzin G (2001) Computations of transonic flow with the $v^2 - f$ turbulence model. Int J Heat Fluid Flow 22(1):53–61
26. Manceau R, Hanjalić K (2002) Elliptic blending model: a new near-wall reynolds-stress turbulence closure. Phys Fluids 14(2):744–754
27. Javadi A Implementation of Elliptic Blending Reynolds Stress model in OpenFOAM, Technical internal report in CFD with Open software course
28. Thielen L, Hanjalić K, Jonker H, Manceau R (2005) Predictions of flow and heat transfer in multiple impinging jets with an elliptic-blending second-moment closure. Int J Heat Mass Transfer 48(8):1583–1598
29. Nicoud F, Ducros F (1999) Subgrid-scale stress modelling based on the square of the velocity gradient tensor. Flow Turbul Combust 62(3):183–200. https://doi.org/10.1023/A:1009995426001
30. Schumann U (1975) Subgrid scale model for finite difference simulations of turbulent flows in plane channels and annuli. J Comput Phys 18(4):376–404
31. Pope SB (2001) Turbulent flows. Cambridge University Press, Cambridge. http://www.cambridge.org/catalogue/catalogue.asp?isbn=0521598869
32. Lund TS, Wu X, Squires KD (1998) Generation of turbulent inflow data for spatially-developing boundary layer simulations. J Comput Phys 140(2):233–258. https://doi.org/10.1006/jcph.1998.5882
33. Klein M, Sadiki A, Janicka J (2003) A digital filter based generation of inflow data for spatially developing direct numerical or large eddy simulations. J Comput Phys 186:652–665. https://doi.org/10.1016/S0021-9991(03)00090-1
34. Wang C, Luo L, Wang L, Sundén B (2016) Effects of vortex generators on the jet impingement heat transfer at different cross-flow reynolds numbers. Int J Heat Mass Transfer 96:278–286
35. Barata JM, Neves FM, Vieira DF, Silva AR et al (2014) Experimental study of two impinging jets aligned with a cross-flow. J Mod Phys 5(16):1779

Publisher's note Springer Nature remains neutral with regard to jurisdictional claims in published maps and institutional affiliations.